



Politecnico  
di Bari

Repository Istituzionale dei Prodotti della Ricerca del Politecnico di Bari

Modeling and experimental analysis of fiber laser offset welding of Al-Ti butt joints

This is a pre-print of the following article

*Original Citation:*

Modeling and experimental analysis of fiber laser offset welding of Al-Ti butt joints / Casalino, Giuseppe; Mortello, Michelangelo. - In: INTERNATIONAL JOURNAL, ADVANCED MANUFACTURING TECHNOLOGY. - ISSN 0268-3768. - STAMPA. - 83:1-4(2017), pp. 89-98. [10.1007/s00170-015-7562-8]

*Availability:*

This version is available at <http://hdl.handle.net/11589/62868> since: 2021-04-11

*Published version*

DOI:10.1007/s00170-015-7562-8

Publisher:

*Terms of use:*

(Article begins on next page)

# International Journal of Advanced Manufacturing Technology

## Modeling and experimental analysis of fiber laser offset welding of Al-Ti butt joints.

--Manuscript Draft--

<b>Manuscript Number:</b>	JAMT-D-15-00233R1
<b>Full Title:</b>	Modeling and experimental analysis of fiber laser offset welding of Al-Ti butt joints.
<b>Article Type:</b>	Original Research
<b>Keywords:</b>	laser welding; off-set; Al-Ti weld; FEM analysis.
<b>Corresponding Author:</b>	Michelangelo Mortello Politecnico di Bari bari, ITALY
<b>Corresponding Author Secondary Information:</b>	
<b>Corresponding Author's Institution:</b>	Politecnico di Bari
<b>Corresponding Author's Secondary Institution:</b>	
<b>First Author:</b>	Michelangelo Mortello
<b>First Author Secondary Information:</b>	
<b>Order of Authors:</b>	Michelangelo Mortello Giuseppe Casalino, professor
<b>Order of Authors Secondary Information:</b>	
<b>Funding Information:</b>	
<b>Abstract:</b>	In spite of great potentiality in aircraft and automotive industries, dissimilar joining of hybrid Al-Ti structures is often challenging because of the unavoidable formation of brittle intermetallic compounds, mixing of molten phases and large differences in material properties. In this work dissimilar 2 mm thickness AA5754 and Ti6Al4V butt joints were produced by shifting an Yb fiber laser source on the upper surface of the Ti sheet. Neither filler wire nor groove preparation was adopted. Different working conditions and seam shapes were assessed. Results, characterized in terms of microstructure, micro-hardness and tensile behavior, showed good characteristics and margins for improvement. The finite element analysis supported the investigation and provided temperature distribution and thermal cycle in the work-piece. The calculation was carried out by ANSYS parametric design language (APDL). Temperatures and seam cross section were detected for validating the model. Numerical output approached experimental results with good accuracy

## **Reviewer #1**

Section headings were corrected as you suggested.

## **Reviewer #2**

1. I deleted the commercial name of the machine as you suggested.
2. Resolution of pictures 5, 6, and 7 has been improved.
3. In the introduction, three references [13, 15, 16] were added to demonstrate that bead appearance and mechanical properties were improved by shifting the laser beam on the Ti upper surface with respect to the literature.

Conclusions were modified accordingly.

Dear Editor,

I made some changes to the paper following your and referees' comments.

Each change has been explained in the file for referees and editor.

Sincerely

Michelangelo Mortello

# Modeling and experimental analysis of fiber laser offset welding of Al-Ti butt joints

Giuseppe Casalino<sup>1</sup>, Michelangelo Mortello<sup>1,\*</sup>

<sup>1</sup>Politecnico di Bari, Dipartimento di Meccanica Matematica e Management (DMMM)

\*Corresponding author: Michelangelo Mortello

Telephone: 00390805962753

E-mail address: [Michelangelo.mortello@poliba.it](mailto:Michelangelo.mortello@poliba.it).

## Abstract

In spite of great potentiality in aircraft and automotive industries, dissimilar joining of hybrid Al-Ti structures is often challenging because of the unavoidable formation of brittle intermetallic compounds, mixing of molten phases and large differences in material properties. In this work dissimilar 2 mm thickness AA5754 and Ti6Al4V butt joints were produced by shifting an Yb fiber laser source on the upper surface of the Ti sheet. Neither filler wire nor groove preparation was adopted. Different working conditions and seam shapes were assessed. Results, characterized in terms of microstructure, micro-hardness and tensile behavior, showed good characteristics and margins for improvement. The finite element analysis supported the investigation and provided temperature distribution and thermal cycle in the work-piece. The calculation was carried out by ANSYS parametric design language (APDL). Temperatures and seam cross section were detected for validating the model. Numerical output approached experimental results with good accuracy.

**Key-words:** laser welding; off-set; Al-Ti weld; FEM analysis.

## 1. Introduction

During the last years, because of environmental and economic requirements, the industries are requested to develop new technological solutions and customized materials, in order to promote costs reduction and conservation of resources. Multi-materials heterogeneous assemblies combine constructively the main advantages of each component into an advanced material, capable to work

in heterogeneous conditions, preserve waste of material and reduce the weight of the whole structure [1]. In particular, Al-Ti lightweight hybrid structures have a wide range of applications and potential prospects in aerospace, aircraft and automotive industries, for which reduction of weight and fuel consumption represents a basic requirement [2, 3]. Whereas Al presents lower density, reduced costs and sheet forming properties, Ti boasts excellent corrosion properties, biocompatibility, higher tensile strength and good high- temperature behavior [4, 5]. Al-Ti structure is already used in several wings of airplanes, in which the Al honeycomb is welded to the Ti crust. Another example is the seat-track in the aircraft: it is suggested to use Ti instead of Al for the fabrication of the imperiled area of the seat-track, in order to prevent corrosion, which basically acts on the elements in the cabin [6]. Mechanical joining techniques, such as riveting, screwing and clinching are currently the most used because they do not require metallurgical compatibility between the materials joined. The assembly of Al to Ti results difficult when applying the traditional fusion methods due to their large difference in thermophysical properties (melting point, heat conductivity, etc.), limited mutual solubility, mixing of melted phases and formation of extended brittle intermetallic compound layers. Uncontrolled growth of intermetallic phases weakens the mechanical behavior and favors the initiation and propagation of cracks [7]. Figure 1 shows the Ti-Al binary phase diagram.

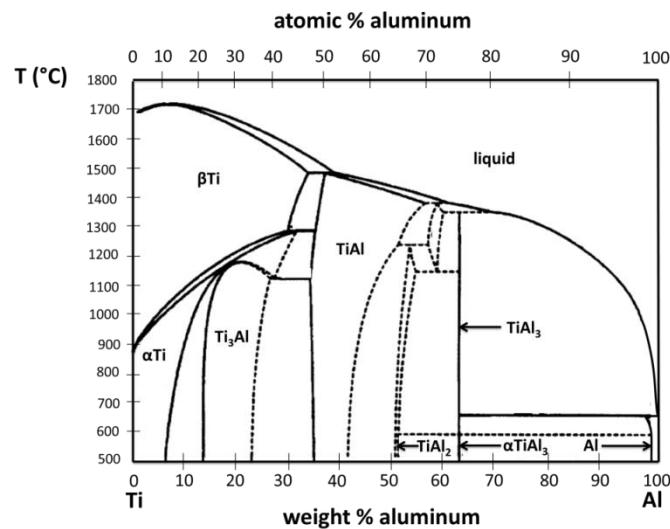


**Fig.1** Ti-Al Binary phase diagram

Although the formation of intermetallic phases depends on process-related temperature-time cycles, which are associated to non-equilibrium phenomena, several elements could be inferred from the equilibrium diagram. Depending on chemical composition, various intermetallic compounds form (TiAl<sub>3</sub>, TiAl, TiAl<sub>2</sub>, Ti<sub>3</sub>Al,) and, among them, TiAl<sub>3</sub> is thermodynamically and kinetically more favorable to be achieved [8]. Dissimilar metals are demanded to have some degree of mutual

1 solubility in order to promote the feasibility of fusion welded joints. The diagram shows a solid  
2 solution up to about 13 at% towards Ti rich side, whereas the early formation of  $TiAl_3$  occurs when  
3 the Ti content exceeds approximately the 2 at% on the Al rich side of the diagram. Compared with  
4 other fusion techniques, fiber laser welding can be considered as a desirable thermal source for  
5 controlling interfacial reaction layer, thanks to its locally restricted high energy input and high  
6 process speed [9]. Lee et al. demonstrated that the combination of high welding speed and high  
7 energy density could suppress the growth of the intermetallic zone [10]. Casalino et al studied the  
8 hybrid laser welding process for joining molten to laser sintered austenitic stainless steels [11]. In  
9 many studies laser welded dissimilar Al-Ti joints were performed by shifting the source on the  
10 substrate of the Al side, which presents a lower melting point. As examined by Khoshhal et al.,  
11 when a Ti sheet is immersed in a Al molten bath, both Ti and Al diffuse into each other [12]. Chen  
12 et al. observed cracks initiation and propagation in order to find the interfacial reaction layer  
13 morphologies that enhance mechanical properties [13]. Song et al. found that, with increasing of the  
14 laser offset, the maximum temperature at the interface becomes lower and the time for diffusion of  
15 Ti atoms decreases giving a thinner layer [14]. Tomashchuk et al. demonstrated that positioning the  
16 laser beam on the Al sheet and maximizing cooling gradient limit inter-diffusion and mixing of  
17 melted materials [15]. Vaidya et al. performed laser welded dissimilar joints by inserting the Ti  
18 sheet into profiled Al sheet in order to favor the coupling [16]. Because of the mixing of liquid  
19 phases and the excessive growth of brittle structures, the traditional fusion welding provokes  
20 reduction of mechanical properties and high seam defectiveness [15]. Moreover, in several studies  
21 accurate groove preparations and filler wire are required [13, 16]. Thus, novel techniques and  
22 procedures should be developed with the aim to perform high quality customized dissimilar  
23 assembly and high productivity joining process. A full comprehension and optimization of joining  
24 process could be achieved by supporting the analysis with a FEM simulation. Moreover, this  
25 increases the productivity for manufacturing industries and favors the analysis of aspects which  
26 cannot be understood by analytical methods. Chen et al. studied the interfacial reaction non-  
27 homogeneity by using FEM method [17]. Kreimeyer et al. adopted the numerical simulation to pre-  
28 determine process parameters and thermal cycles required [18]. In this work, the fiber laser offset  
29 welding (FLOW) of dissimilar Al-Ti joints in butt configuration was conducted by focusing the  
30 laser beam on the top surface of the Ti sheet. The keyhole melted Ti by direct irradiation and the  
31 heat conduction promoted the joining at the interface. Two different kinds of interfacial reaction  
32 layers were presented. Compared to results found in literature, this procedure increased the  
33 mechanical properties of the welds. A FEM model was implemented by modeling the thermo-

mechanical behavior of the laser source. Temperature fields and thermal cycles were assessed to validate the model. Numerical data approached experimental observations with good accuracy.

## 2. Modeling and analysis

### 2.1 Experimental

Ti6Al4V and AA5754 plates with a thickness of 2 mm were joined in butt configuration. The chemical composition, mechanical properties and thermo-physical properties of the two alloys are listed in tables 1, 2 and 3, respectively.

**Table 1** Chemical composition of the as-received materials (weight %).

	Ti	Al	H	Fe	O	N	C	V	W	Other
<b>Ti6Al4V</b>	Balance	6.10	0.01	0.05	0.20	0.05	0.10	4.00	0.30	0.40

**Table 2** Mechanical properties of the as-received materials: ultimate tensile strength (UTS), yield stress (YS), Young module (E), elongation to fracture %( A %), Vickers microhardness (HV).

	UTS (MPa)	YS (MPa)	E (GPa)	A%	HV
<b>Ti6Al4V</b>	950	880	114	14	349
<b>AA5754</b>	230	80	68	17	62

**Table 3** Thermo-physical properties of the two base materials: thermal conductivity (K), melting temperature(Tm), density ( $\rho$ ).

	K (W/(m.K))	Tm (k)	$\rho$ (g/ cm <sup>3</sup> )
<b>Ti6Al4V</b>	6.7	1650	4.43
<b>AA5754</b>	147	870	2.66

Prior to welding sheets were prepared by cutting (low-speed milling), polishing (200 grit sandpaper) and cleaning (acetone), in order to improve the surface contact. An Yb fiber laser was used in continuous wave regime by exploiting a 200  $\mu$ m diameter optical fiber. Collimating lens and focusing lens with a focal length of 120 mm 250 mm respectively were used to deliver the beam on

the top surface of the work-piece. A focus spot of about 300  $\mu\text{m}$  diameter ( $1/e^2$  width) near-Gaussian distribution was produced. The irradiation of Al alloys, due to prohibitive optical and thermo-physical material properties, is compromised by the obvious tendency to keyhole instability. This favors geometric defects, loss of alloying elements, porosity and cracking [19]. So the laser beam was shifted on the Ti plate upper surface with the aim to generate the keyhole. Hence Ti base metal was melted by direct irradiation, while Al base metal was melted via heat conduction through the interface. Since diffusion starts at modest temperature already (less than 600  $^{\circ}\text{C}$ ), it was intended to limit the heat input in such a way that the Ti close to the interface was not melted. As a consequence the excessive growth of IMC layer was avoided. Fig. 2 shows a schematic illustration of the FLOW layout. Fuse zones (FZ) and heat affected zones (HAZ) are indicated in the work-piece. The distance between the center of the laser focus spot and the contact surfaces was called “laser offset”. Casalino et al. performed Ti T40 and AA5754 off-set welding using a disk laser [20].

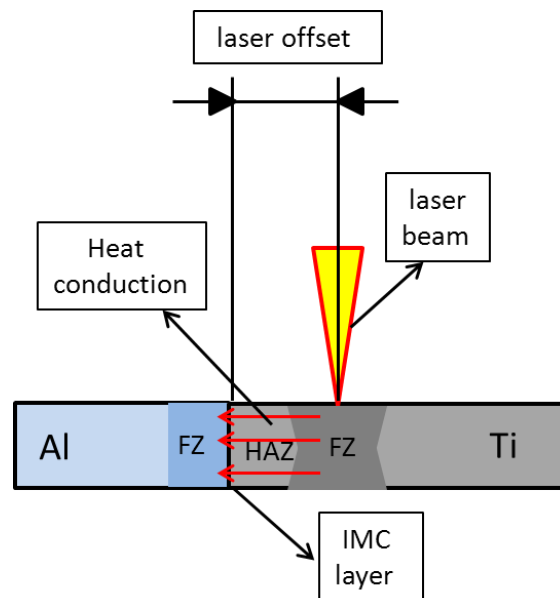


**Fig.2** Laser offset welding configuration for Al-Ti dissimilar butt joints

Neither filler wire nor groove preparation was adopted. During the welding the bath was double shielded on both the upper and bottom surfaces using Ar gas with a flow rate of 15 l/min. This prevents contaminations by solid particles and absorption of harmful atmosphere gases [21]. Prior to carrying out the analysis preliminary tests were conducted for the determination of the window of admissible process parameters.

The laser offset was kept constant at 0.75 mm. The heat input was defined in term of linear energy (LE) as the ratio between the laser power and the welding speed. The values of the process

parameters varied are listed in table 4. The corresponding linear energy was calculated for each welding condition.

**Table 4** Process parameters adopted.

Sample	Laser power (kW)	Welding speed (m/min)	Linear energy (J/mm)
1	1.20	1.00	70.60
2	1.20	2.00	35.30
3	1.50	2.50	35.70
4	1.50	3.00	30.00

After verifying the soundness of assemblies, joints were cross-sectioned perpendicularly to the welding direction, polished with standard grinding procedures and chemically etched by Keller's reagents solution (1% HF, 1.5% HCl, 2.5% HNO<sub>3</sub> and 95% H<sub>2</sub>O). Microstructure was assessed through optical microscopy (OM) and scanning electron microscopy (SEM) equipped with energy-dispersive X-ray spectrometer (EDS). Vickers micro-hardness was measured at the mid thickness of the cross section. A load time of 20 s and a test load of 200 g were adopted. The distance between two neighboring indentations was kept equal to 0.25 mm. Three specimens with a 20 mm width were cut from each joint in order to assess the mechanical behavior of the welds. An INSTRON 5881 testing machine was used at room temperature by adopting a 10<sup>-4</sup> s<sup>-1</sup> strain rate. The average values of tensile strength and elongation % were compared to evaluate which welding conditions enhance mechanical properties of welds.

## 2.2 Modeling

FEM analysis was conducted by using parametric design language (APDL) available in the ANSYS finite element code. The following purposes were established:

- The determination of the thermal cycles and the temperature fields in the work-pieces in order to support the thermo-dynamic analysis of microstructures.
- The prediction of the system thermo-mechanical behavior and pool shape, under assigned working conditions.

- The optimization of the process parameters supporting analytical methods. This reduces the time required for a full analysis.

An eight-nodes quadratic three dimensional solid element SOLID 70 was chosen to carry out the model creation. The laser welding process in keyhole regime was simulated. The modeling of the source was carried out by associating an internal production of thermal load to several specific elements close to the welding line. The selection depended on both the dimension of the capillary (function of the focus spot) and the macrograph of the cross section. The generative internal heat load associated to the elements was defined as the ratio between the total power transmitted and the volume of the element. Nodes were selected in a double-spherical local system. Prior to carrying out the study convergence tests were conducted to find a suitable number of elements for modeling the plates. A finer mesh was generated near the seam zone, where the temperature and cooling rate gradients are more relevant and the thermal behavior is more critical. Thermal resistance at the contact interfaces was simulated by inserting a thin layer of low-conductivity elements. As concerns boundary conditions the following main assumptions were made:

- Thermo-physical properties of the materials were assumed to be isotropic and temperature-dependent according standard values found in literature. The behavior at the molten state was estimated by comparing with experimental results.
- Energy losses due to slow air convection were assumed equal to  $20 \text{ W/m}^2\text{K}$ .
- Irradiation, convective melt flow, buoyancy forces and viscous forces were reasonably neglected.
- The environmental temperature at the starting condition was assumed to be equal to  $20 \text{ (}^\circ\text{C)}$ .

Nodal temperature history was obtained by introducing the source motion during the process. DO\* cycle loop was used to simulate the thermo-dynamic behavior of the system in a finite number of subsequent steps. The thermal load was associated at the beginning of each step and temperature fields were re-calculated at every step starting. The time required for each step corresponds to the ratio between the step increment and the welding speed. Thermal cycles achieved were compared to experimental curves. These were detected through the use of thermo-couples positioned 2 mm far from the welding line on both the sheets.

### 3. Results and discussion

#### 3.1 Bead appearance

Figures 3 and 4 show the cross sections of samples 1 and 2, respectively. The examination with optical microscopy revealed the presence of easily discernible zones, detectable by color. Laser offset and thermal input values are the key-parameters of the FLOW process. As listed in table 4, samples 1 and 2 were produced with different values of linear energy (70.60 versus 15.30 J/mm), at fixed laser offset (0.75 mm). Because of the large disparity in heat input, the seam morphology and the joining thermo-dynamic resulted to be very different.

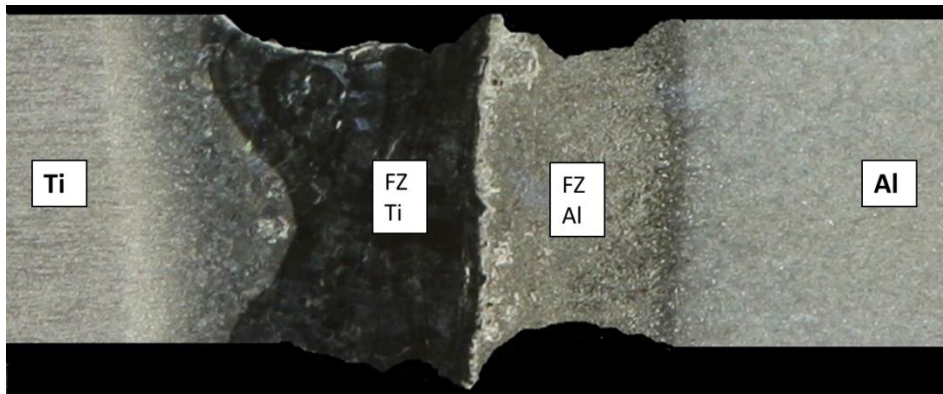


Fig.3 Macrograph of sample 1 (P=1.20 kW, v=1 m/min, LE= 70.60 J/mm, offset= 0.75 mm)

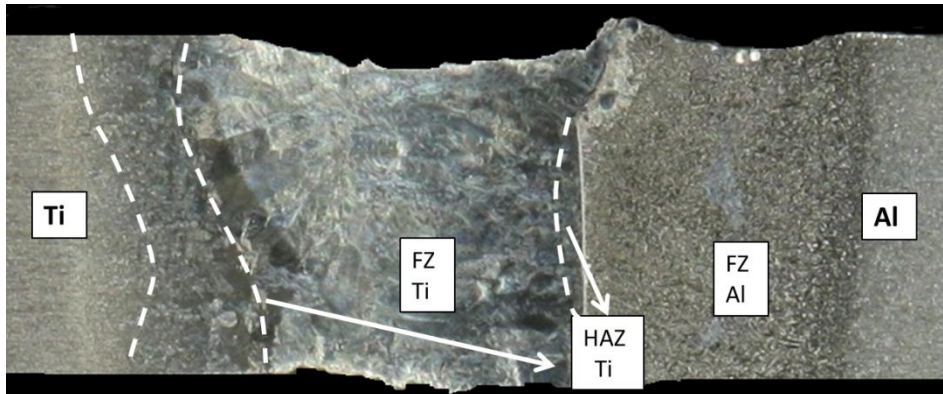


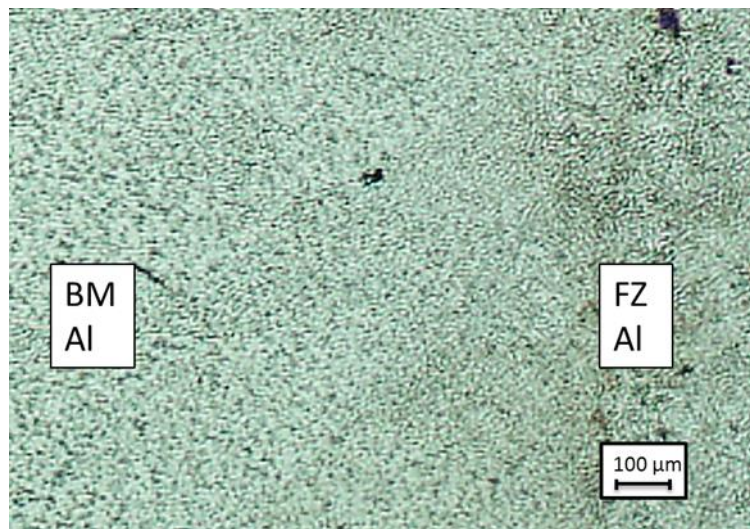
Fig.4 Macrograph of sample 2 (P=1.20 kW, v=2 m/min, LE= 35.30 J/mm, offset= 0.75 mm)

Figure 3 shows the cross section of sample 1. A high value of linear energy provoked a too extended Ti FZ width, which reached the Al FZ. Mixing of phases and alteration of the interface linearity occurred because of the interaction between two liquid-state materials. Moreover, the over-heating of the Ti bath favored geometrical defectiveness, such as distortions, underfill, excessive penetration and reduction of the cross section thickness in proximity to the interface. The

1 uncontrolled growth of interface reaction layer caused an excessive formation of brittle phases in  
2 the seam [13]. In fact, due to diffusion above the Al recrystallization temperature intermetallic  
3 phases have too much time to grow considerably [14]. Loss of ductility, residual stresses and  
4 different thermal expansion coefficients favored cracking, which can be observed mostly in the Al  
5 side of the weld [22]. On the other hand, figure 4 presents the seam morphology of the cross section  
6 of sample 2. The lower heat input transmitted was not sufficient to melt the Ti base alloy in  
7 proximity to the Al side of the joint. So the molten Al wet solid Ti sheet generating a HAZ in the Ti  
8 side. The growth of interfacial reaction layer was limited and cracking was prevented. The linearity  
9 of the interface was preserved thanks to the action of the solid-state Ti that hindered the melted Al  
10 flow towards the Ti side. Geometrical defectiveness was significantly lower comparing with sample  
11 1.  
12  
13  
14  
15  
16  
17  
18  
19  
20  
21  
22

### 23 3.2 Microstructure

24  
25 The evolution in microstructure of the as-received materials can be observed in figures 5 and 6. At  
26 first, figure 5 shows that the grain size of Al alloy decreased in comparison with the parent metal.  
27 Al plate was melted due to the heat conduction in the work-piece. Because of the rapid  
28 heating/cooling cycles, the growth of dendrites was limited by the precipitation of inter-granular Mg  
29 at the grain boundaries [23].  
30  
31  
32  
33  
34  
35

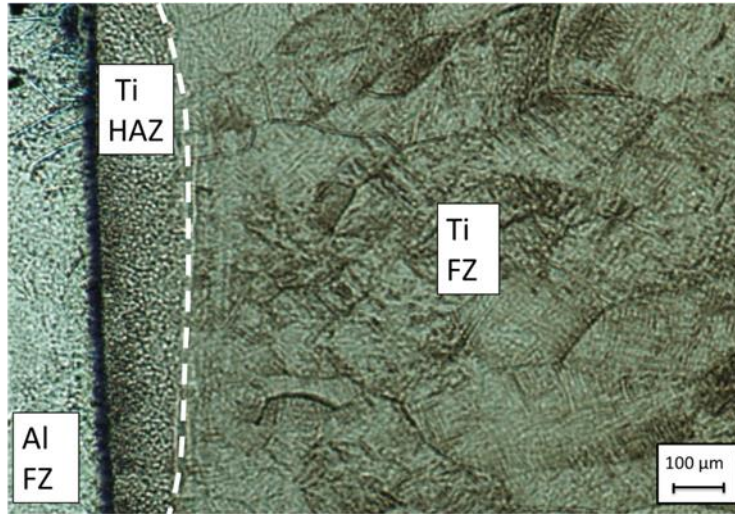


53 **Fig.5.** Microstructure of the Al side of sample 2 (P=1.20 kW, v=2 m/min, LE= 35.30 J/mm, offset= 0.75 mm).  
54  
55  
56  
57

58 Figure 6 shows that, after the welding, the Ti alloy microstructure was made up of two different  
59 zones. The HAZ consisted in equiaxed primary  $\alpha$  and inter-granular  $\beta$  phases, whereas the FZ was  
60  
61  
62  
63  
64  
65

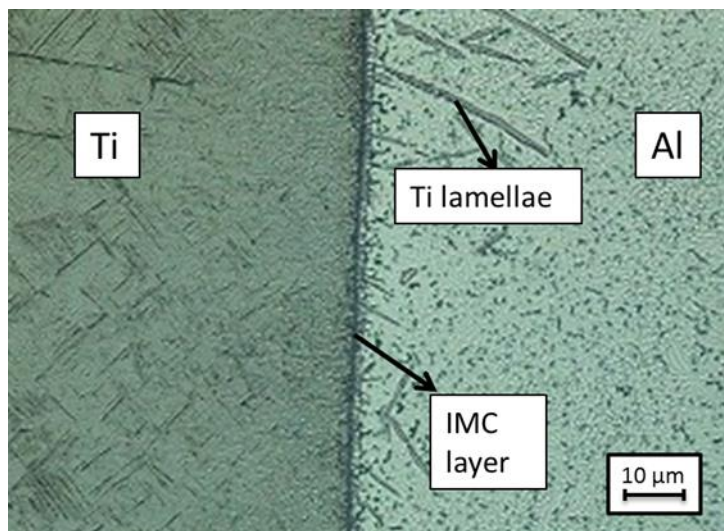
1  
2  
3  
4  
5  
6  
7  
8  
9  
10  
11  
12  
13  
14  
15  
16  
17  
18  
19  
20  
21  
22  
23  
24  
25  
26  
27  
28  
29  
30  
31  
32  
33  
34  
35  
36  
37  
38  
39  
40  
41  
42  
43  
44  
45  
46  
47  
48  
49  
50  
51  
52  
53  
54  
55  
56  
57  
58  
59  
60  
61  
62  
63  
64  
65

composed of equi-axed  $\alpha$ , retained  $\beta$  and acicular martensite  $\alpha^1$ , which was generated because of the high cooling rate [24]. Dendrites grew in the direction of the thermal flow.



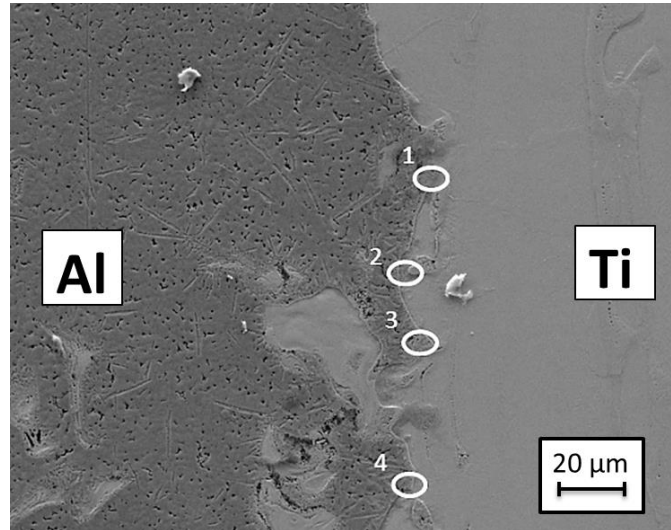
**Fig.6** Microstructure of the Ti side of sample 2 (P=1.20 kW, v=2 m/min, LE= 35.30 J/mm, offset= 0.75 mm)

Figure 7 shows the interface layer morphology of sample 2. IMC layer, limited to few microns thickness, appeared homogeneous and linear thanks to the low thermal input. Ti lamellae diffused in the Al matrix above the Al recrystallization temperature. They developed in the direction of the thermal flows for an extension approximately between 1-2 μm and more than 20 μm. Neither pores nor cracks were observed thanks to the optimal thermal input.



**Fig.7** IMC layer of sample 2 (P=1.20 kW, v=2 m/min, LE= 35.30 J/mm, offset= 0.75 mm)

Figure 8 shows the optical observation of sample 1 achieved by SEM with a magnification of 1000x. White circles indicate the regions analyzed with the EDS. A morphological investigation and element mapping analysis were conducted. The results of chemical composition are listed in table 5.



**Fig.8** IMC layer of sample 1 detected through SEM (P=1.20 kW, v=1 m/min, LE= 70.60 J/mm, offset= 0.75 mm)

**Table 5** Chemical composition of the zones indicated in figure 8.

Zone	Al	Mg	Ti	V
1	73.5	1.1	24.0	1.4
2	88.0	3.1	8.5	0.3
3	53.6	0.9	43.2	2.3
4	52.2	1.5	40.9	2.4

The interface reaction layer appeared curvilinear and non-homogeneous because of the high thermal input and the consequent interaction between liquid-state materials. Ti lamellae cross the Al alloy side, as found in figure 7. Micro-cracks were detected in the Al side close to the interface. They were probably due to residual stresses and brittleness of the interface layer. As found in literature, various intermetallic phases (TiAl, TiAl<sub>3</sub>, TiAl<sub>2</sub> and Ti<sub>3</sub>Al) are distributed irregularly at interfacial zone, because of concentration and temperature gradients [25]. In fact the intermetallic layer was made up of a complex sequence of different compounds with an uneven distribution. The chemical composition analysis revealed that the IMC was made up of both Ti and Al atoms with a certain gradient of concentration. However, it is not possible to determine, through the EDS, the precise distributions of each compound in the whole examined area.

1  
2  
3  
4  
5  
6  
7  
8  
9  
10  
11  
12  
13  
14  
15  
16  
17  
18  
19  
20  
21  
22  
23  
24  
25  
26  
27  
28  
29  
30  
31  
32  
33  
34  
35  
36  
37  
38  
39  
40  
41  
42  
43  
44  
45  
46  
47  
48  
49  
50  
51  
52  
53  
54  
55  
56  
57  
58  
59  
60  
61  
62  
63  
64  
65

### 3.3 Tensile strength

The histograms of the average ultimate tensile strengths and elongations % are shown in figures 9 and 10, respectively.

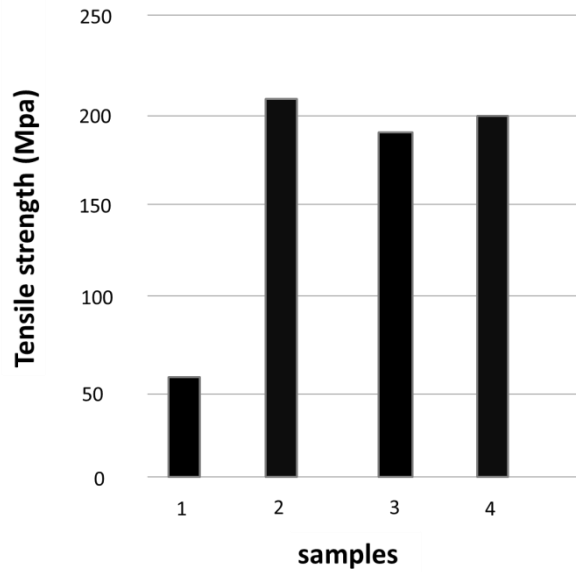


Fig.9 Average values of tensile strength of samples

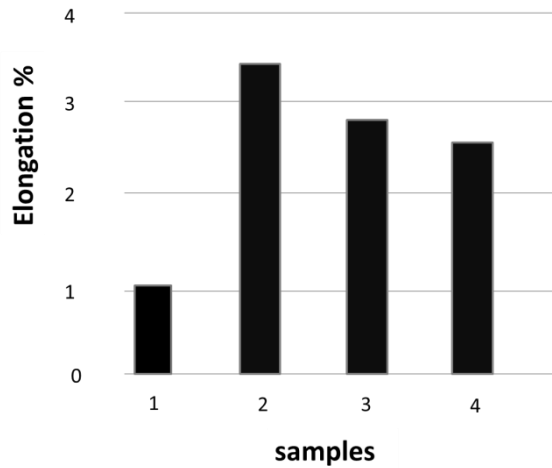


Fig.10 Average values of elongation % of sample

The mechanical behavior of Al-Ti dissimilar joints was compromised by the unavoidable formation of brittle intermetallic compounds in the interface layer [7, 14]. The tensile strength of samples

performed with appropriate combination of process parameters reached almost the 90 % of that typical of the parent metal (see table 2). The loss of ductility was more drastic due to the brittleness of IMC. Sample 2, 3 and 4 resulted to be more resistant and ductile, because the IMC layer was as thin as to prevent the expansion of brittle phases. As shown in table 4, sample 1 was performed with a significantly higher value of linear energy. As discussed in details, the excessive thermal input promoted an uncontrolled growth of interfacial reaction layer and mixing of melted phases. This condition favored the formation of brittle structures and cracks in proximity to the interface. Moreover thick reaction layers increase residual stresses and promote crack and micro-voids initiation [17]. Under tensile load, when local stresses reached the maximum strength of the material, cracks propagated leading to structure failure. Therefore the condition for which molten Al alloy wets the solid state Ti alloy enhances the mechanical properties of joints performed by FLOW technique.

### 3.4 Microhardness

Figure 11 shows the micro-hardness profile detected from the cross section of sample 2 at the mid thickness. Closed values were found for all operational conditions.

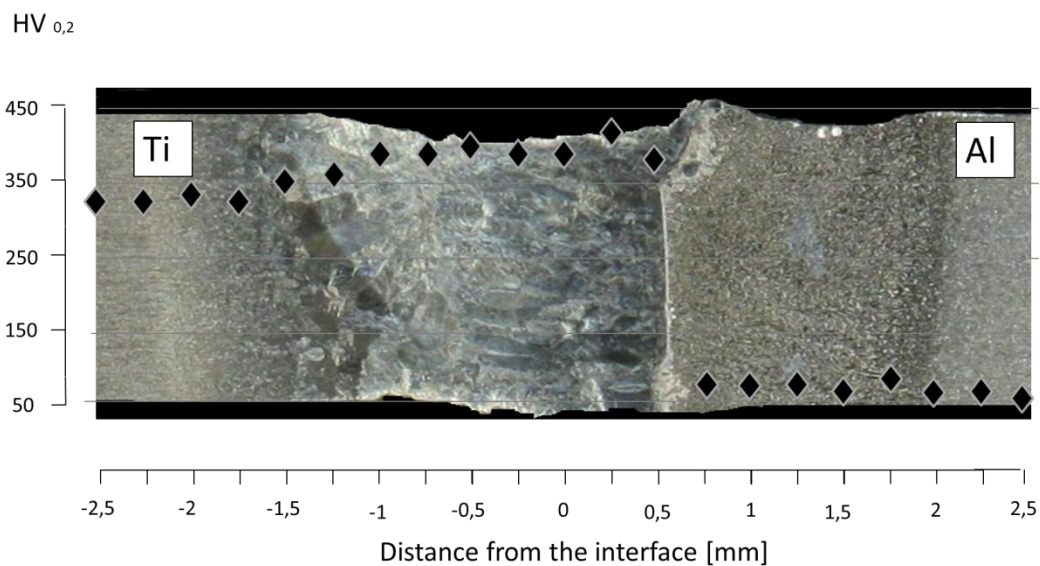


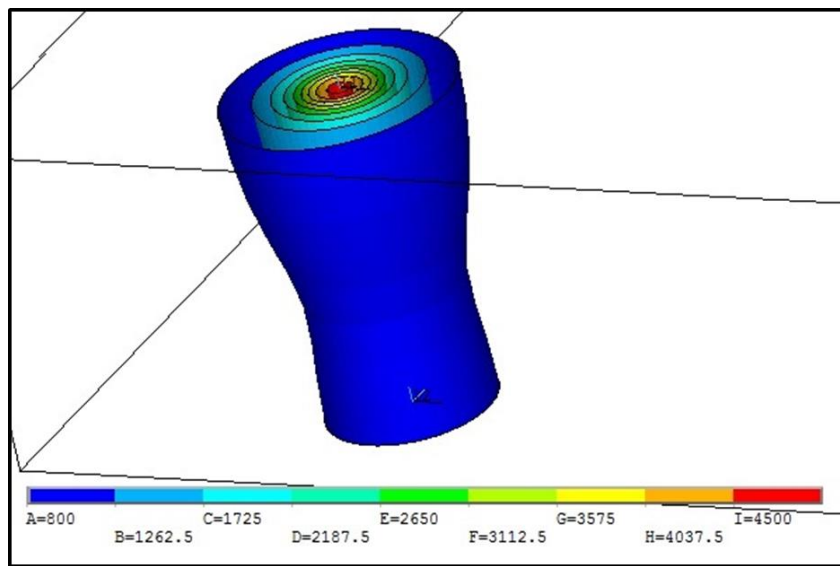
**Fig.11** Microhardness profile detected at the mid thickness

A slight increase of hardness was registered in the FZ of the Al alloy because of the refined grain sizes after the precipitation of solid state inter-granular Mg at the Al grain boundaries. So a precipitation hardening occurred. An increase of hardness of about the 15% was detected in the FZ of the Ti side. It was due to the presence of the acicular martensitic structure  $\alpha^1$  achieved because of

1 the rapid cooling rate. It was not possible to evaluate the hardness value at the interface because the  
2 IMC layer was not as large to allow the indenter of the machine to test the resistance to penetration  
3 of the material properly. So nano-indentations occur.  
4  
5  
6  
7

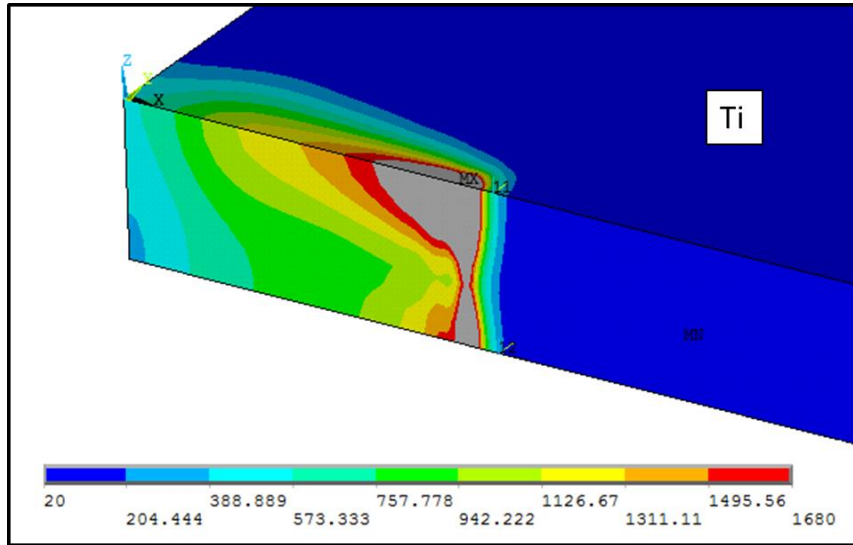
### 8 **3.5 Thermal analysis results**

9  
10 The temperature fields in the Ti sheet under a singular thermal load step condition are presented in  
11 figure 12. Temperature iso-surfaces are shown in a three-dimensional representation. The  
12 temperature decreases with the increasing distance from the thermal load. The temperature  
13 distribution is not symmetric in the thickness of the sheet because the selection of nodes depended  
14 on both the dimension of capillary and experimental seam appearance. Temperature values reach  
15 more than 4500 °C in the center of the capillary, in order to reply the plasma thermal behavior.  
16  
17  
18  
19  
20  
21  
22  
23  
24



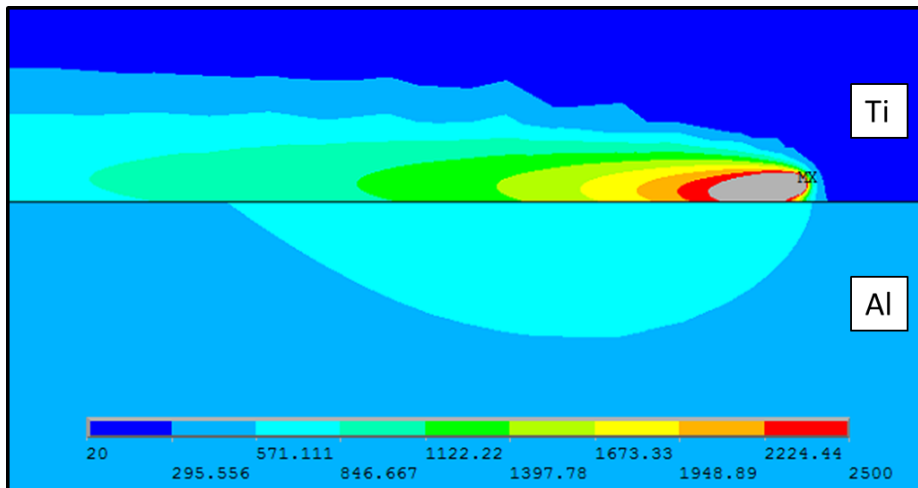
45 **Fig.12** Temperature fields for a singular thermal load application

46  
47  
48  
49  
50 Figure 13 shows the temperature fields in the longitudinal section of the Ti sheet for a fixed instant  
51 of time under the condition of moving source. Temperature fields, calculated for each step, were  
52 influenced by the previous thermal condition. In this way an elliptical temperature distribution in  
53 the planes parallel to the surfaces of the work-piece was achieved.  
54  
55  
56  
57  
58  
59  
60  
61  
62  
63  
64  
65



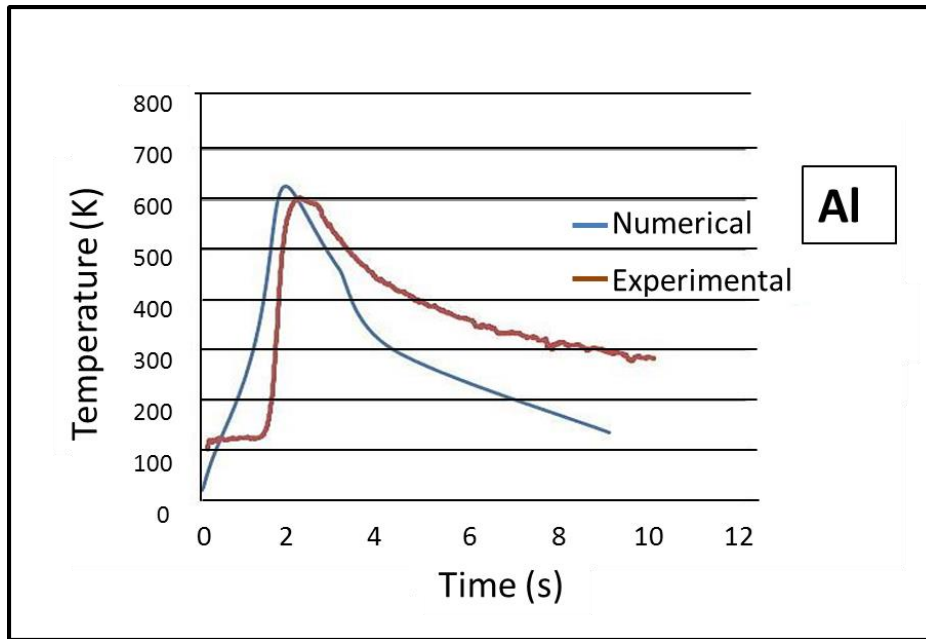
**Fig.13** Temperature distribution in the longitudinal plan under the condition of moving source

Figure 14 shows the temperature distributions on the top surface of an Al-Ti butt joint. The condition for which two molten materials interact was simulated. The large difference in thermo-physical properties and the presence of a thermal resistance at the interface promoted a great gap in the thermal behavior of the two sheets.



**Fig.14** Temperature fields on the top surface of the Al-Ti joint

Figures 15 and 16 show the thermal cycles detected for validating the numerical model, referring to Al side and Ti side, respectively.



**Fig.15** Experimental and numerical thermal cycle for the Al side

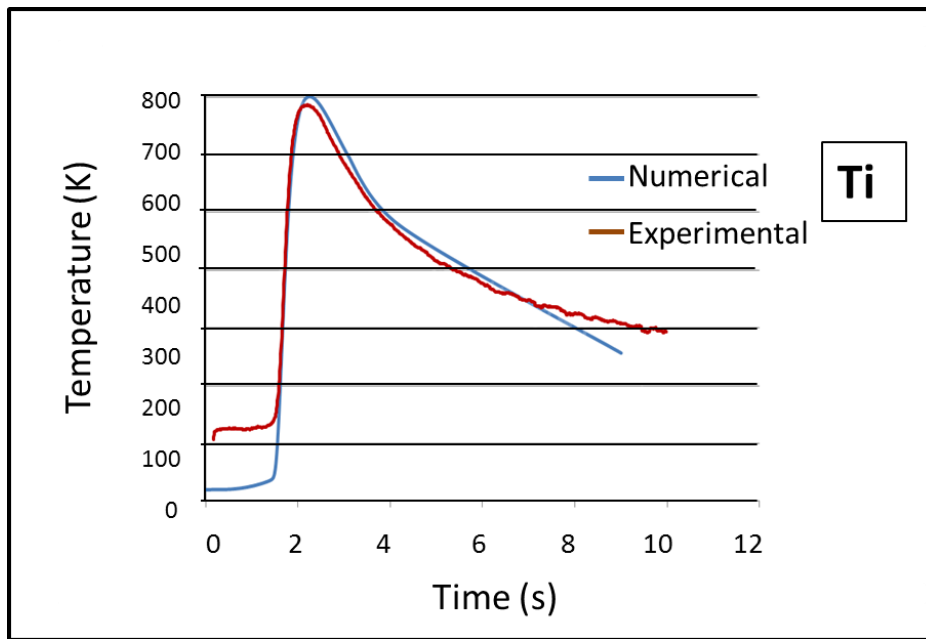


**Fig.16** Experimental and numerical thermal cycle for the Ti side

Both the numerical and the experimental curves are presented for each side of the weld. The former were achieved by simulating the process through FEM analysis, whereas the latter were detected through the thermo-couples measures. The validation of the model was completed by calculating two calibration factors. An iterative procedure was conducted. Numerical results approached the experimental observations. The detailed description of process related thermal cycles was provided

1 at any position in the work-piece. Once the model was calibrated, the working conditions could be  
2 varied in order to assess various temperature distributions at the interface. In this way the  
3 consequent growth of interfacial reaction layer could be controlled with the purpose to produce the  
4 seam morphology that enhances the mechanical behavior of the joint. Besides, the model  
5 implemented allows predicting the pool shape and thermo-dynamic behavior of the pieces, for a  
6 wide range of operative conditions. Moreover the technical limits of analytical methods could be  
7 overcome by combining the experimental investigation with the capabilities of FEM codes [26].  
8 Also the comprehension of microstructure evolution can be supported by evaluating the thermal  
9 distributions in the whole structure for various working conditions.  
10  
11  
12  
13  
14  
15  
16  
17  
18

#### 19 **4. Conclusions**

20 In this work, laser welding was conducted by focusing the laser source on the Ti side of the work-  
21 piece (FLOW). Ti6Al4V and AA5754 alloy with a 2 mm thickness were joined in butt  
22 configuration. Both experimental and numerical analyses were conducted. The following  
23 conclusions are drawn.  
24  
25  
26  
27  
28

- 29 • Good bead appearance and mechanical properties were obtained. Productivity and versatility  
30 of the process was increased.
- 31 • The seam quality and brittle interface depended on both laser offset and linear energy.  
32 Excessive growth of Ti FZ altered the layer homogeneity and favors crack initiation and  
33 propagation. When liquid Al wetted solid Ti the mechanical properties of the joint were  
34 enhanced.
- 35 • The numerical model was accurate and accurately predicted the system thermal behavior  
36 and pool shape geometry under assigned working conditions.
- 37 • Thermal treatments could improve mechanical properties of the welds by recovering  
38 toughness and tensile strength affected by the unavoidable formation of brittle phases.  
39  
40  
41  
42  
43  
44  
45  
46  
47  
48  
49  
50  
51  
52  
53  
54  
55  
56  
57  
58  
59  
60  
61  
62  
63  
64  
65

## References

- [1] Campbell F jr. (2006) Manufacturing technology for aerospace structural materials. Elsevier.
- [2] Bondar A A , Witusiewicz V T, Hecht U, Remez M V, Voblikov V M, Tsyganenko N I, Yevich Ya. I, Podrezov Y M, Velikanova T Y (2011) Structure And Properties Of Titanium–Aluminum Alloys Doped With Niobium And Tantalum. Powder Metallurgy and Metal Ceramics, Vol. 50, Nos. 7-8.
- [3] Woizeschke P, Shumacher J (2013) Failure behavior of aluminum-titanium hybrid seams within a novel aluminum-CFRP joining concept. Physics Procedia Vol. 41; 12–19.
- [4] Miller W S, Zhuang a L, Bottema J, Wittebrood A J, De Smet P, Haszler A, Vieregge A (2000). Recent development in aluminium alloys for the automotive industry. Materials Science and Engineering A280; 37–49.
- [5] Faller K, Froes F H (2001) The Use of Titanium in Family Automobiles: Current Trends. JOM Vol. 53, No. 4; 27-28.
- [6] Moller F, Thomy C, Vollertsen F (2012) Joining of titanium-aluminium seat tracks for aircraft applications-system technology and joint properties. Welding in the world. Vol. 56, Nos. 3-4; 108-114.
- [7] Sambasiva Rao A, Madhusudhan Reddy G, Satya Prasad K (2011) Microstructure and tensile properties of dissimilar metals gas tungsten arc welding of aluminium to titanium alloy. Materials science and technology. Vol. 27, No.1; 65-70.
- [8] Min-Sheng Chu, Shyi-Kaan Wu (2004) Interreactions of TiAl<sub>3</sub> thin film on bulk  $\gamma$ -TiAl and on bulk  $\alpha_2$ -Ti<sub>3</sub>Al alloys at 700-1000°C. Materials transactions. Vol. 45, No.4; 1290-1298.
- [9] Quintino L, Costa A, Miranda R, Yapp D, Kumar V, Kong C J (2007) Welding with high power fiber lasers – A preliminary study. Materials and design. Vol.28, No. 4; 1231-1237.
- [10] Lee S-J, Nakamura H, Kawahito Y, Katayama S (2013) Microstructural characteristics and mechanical properties of single mode fiber laser lap welded joint in Ti and Al dissimilar metal. Transactions of JWRI. Vol. 42, No. 1; 17-21.
- [11] Casalino G, Campanelli S L, Ludovico A D, (2013) Laser-arc hybrid welding of wrought to selective laser molten stainless steel. International journal of advanced manufacturing technology. Vol. 68; 209-216.
- [12] Khoshhal R, Soltanieh M, Mirjalili M (2010) Formation and growth of titanium aluminide layer at the surface of titanium sheets immersed in molten aluminum. Iranian Journal of materials science and engineering. Vol. 7, No. 1; 24-31.
- [13] Chen Y, Chen S, Li L (2010) Influence of interfacial reaction layer morphologies on crack initiation and propagation in Ti/Al joint by laser welding–brazing. Materials and Design. Vol. 31; 227–233.
- [14] Song Z, Nakata K, Wu A, Liao J (2013) Interfacial microstructure and mechanical property of Ti6Al4V/A6061 dissimilar joint by direct laser brazing without filler metal and groove. Materials Science & Engineering A 560; 111–120.
- [15] Tomashchuk I, Sallamand P, Cicala E, Peyre P, Grevey D (2015). Direct keyhole laser welding of aluminum alloy AA5754 to titanium alloy Ti6Al4V. Journal of materials processing technology. A 217; 96-104.

- 1  
2  
3  
4  
5  
6  
7  
8  
9  
10  
11  
12  
13  
14  
15  
16  
17  
18  
19  
20  
21  
22  
23  
24  
25  
26  
27  
28  
29  
30  
31  
32  
33  
34  
35  
36  
37  
38  
39  
40  
41  
42  
43  
44  
45  
46  
47  
48  
49  
50  
51  
52  
53  
54  
55  
56  
57  
58  
59  
60  
61  
62  
63  
64  
65
- [16] Vaidya W V, Horstmann M, Ventzke V, Petrovski B, Kocak M, Kocik R, Tempus G (2010) Improving interfacial properties of a laser beam welded dissimilar joint of aluminum AA6056 and Ti6Al4V for aeronautical applications. *J. Mater. Sci.* A45; 6242-6254.
- [17] Chen S, Li L, Chen Y, Huanga J (2011) Joining mechanism of Ti/Al dissimilar alloys during laser welding-brazing process. *Journal of Alloys and Compounds* A509; 891–898.
- [18] Kreimeyer M, Wagner F, Vollertsen F (2005) Laser processing of aluminum–titanium-tailored blanks. *Optics and Lasers in Engineering* A43; 1021–1035.
- [19] Pastor M, Zhao H, Martukanitz R P, Debroy T (1999) Porosity, Underfill and Magnesium Loss during Continuous Wave Nd:YAG Laser Welding of Thin Plates of Aluminum Alloys 5182 and 5754. *Welding journal.* 78(6); 207-216.
- [20] Casalino G, Mortello M, Peyre P (2015) Yb–YAG laser offset welding of AA5754 and T40 butt joint. *Journal of Materials Processing Technology.* 223; 139–149.
- [21] Akman E, Demir A, Canel T, Sinmazcelik T (2009). Laser welding of Ti6Al4V Ti alloys. *Journal of materials processing technology.* A209; 3705–3713.
- [22] Liedl G, Kratky A, Mayr M, Saliger A (2011) Laser Assisted Joining Of Dissimilar Materials. *IQCMEA-ICF-Processing, Performance and Failure Analysis of Engineering Materials.*
- [23] Farzadi A, Serajzadeh S, Kokabi A H (2010) Investigation of weld pool in aluminum alloys: Geometry and solidification microstructure. *International Journal of Thermal Sciences.* A49; 809-819
- [24] Xiao-Long Gao, Lin-Jie Zhang , Jing Liu, Jian-Xun Zhang (2013) A comparative study of pulsed Nd:YAG laser welding and TIG welding of thin Ti6Al4V titanium alloy plate. *Materials Science & Engineering A* 559; 14–21.
- [25] Bang K-S, Lee K-J, Bang H-S, Bang H-S (2011) Interfacial microstructure and mechanical properties of dissimilar friction stir welds between 6061-T6 aluminum and Ti-6%Al-4%V alloys. *Materials transactions.* Vol. 52; 974-978.
- [26] Möller F, Grden M, Thomy C, Vollertsen F (2011) Combined Laser Beam Welding and Brazing Process for Aluminium Titanium Hybrid Structures. *Physics Procedia* Vol. 12; 215–223.

## List of captions

**Fig.1** Ti-Al Binary phase diagram

**Fig.2** Laser offset welding configuration for Al-Ti dissimilar butt joints

**Fig.3** Macrograph of sample 1 (P=1.20 kW, v=1 m/min, LE= 70.60 J/mm, offset= 0.75 mm)

**Fig.4** Macrograph of sample 2 (P=1.20 kW, v=2 m/min, LE= 35.30 J/mm, offset= 0.75 mm)

**Fig.5.** Microstructure of the Al side of sample 2 (P=1.20 kW, v=2 m/min, LE= 35.30 J/mm, offset= 0.75 mm)

**Fig.6** Microstructure of the Ti side of sample 2 (P=1.20 kW, v=2 m/min, LE= 35.30 J/mm, offset= 0.75 mm)

**Fig.7** IMC layer of sample 2 (P=1.20 kW, v=2 m/min, LE= 35.30 J/mm, offset= 0.75 mm)

**Fig.8** IMC layer of sample 1 detected through SEM (P=1.20 kW, v=1 m/min, LE= 70.60 J/mm, offset= 0.75 mm)

**Fig.9** Average values of tensile strength of samples

**Fig.10** Average values of elongation % of sample

**Fig.11** Microhardness profile detected at the mid thickness

**Fig.12** Temperature fields for a singular thermal load application

**Fig.13** Temperature distribution in the longitudinal plan under the condition of moving source

**Fig.14** Temperature fields on the top surface of the Al-Ti joint

**Fig.15** Experimental and numerical thermal cycle for the Al side

**Fig.16** Experimental and numerical thermal cycle for the Ti side

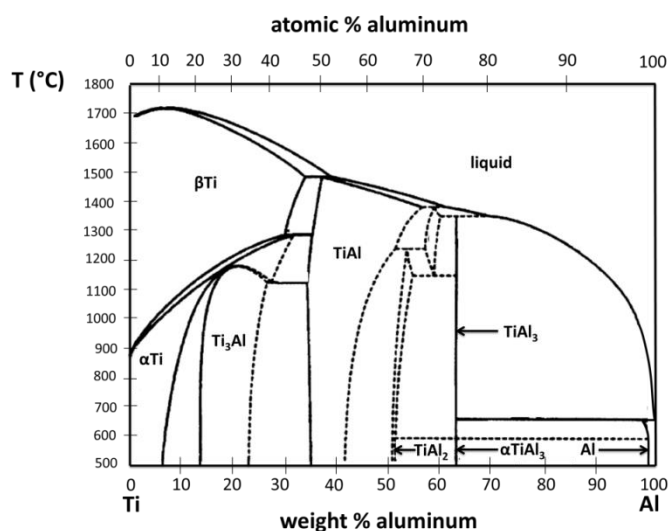


**Fig.1** Ti-Al Binary phase diagram

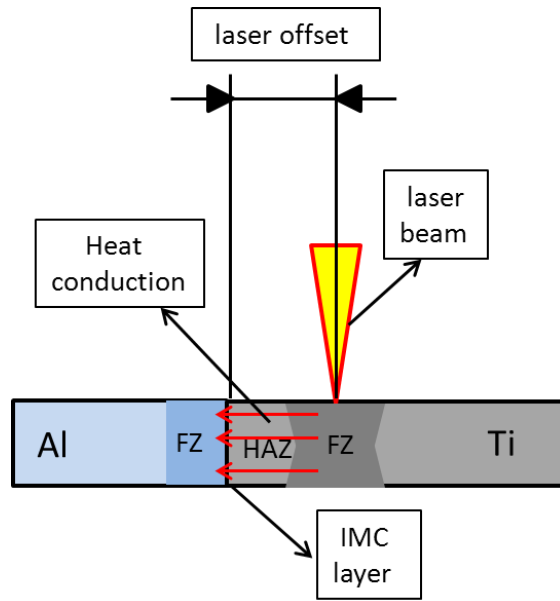


**Fig.2** Laser offset welding configuration for Al-Ti dissimilar butt joints

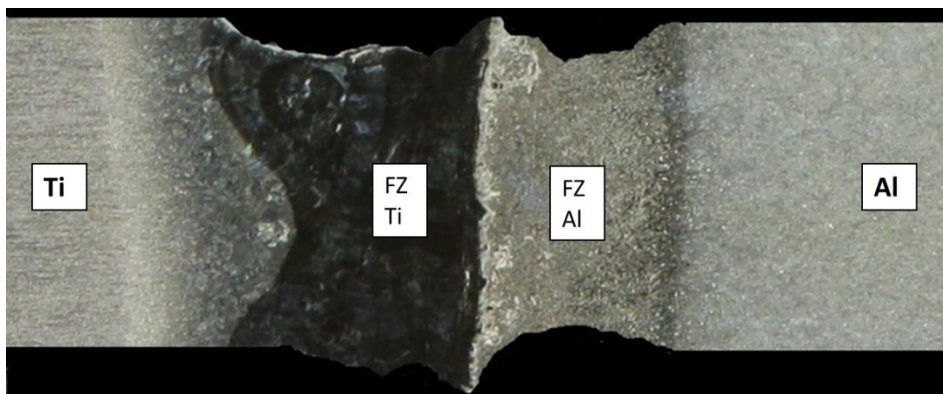


**Fig.3** Macrograph of sample 1 ( $P=1.20$  kW,  $v=1$  m/min,  $LE= 70.60$  J/mm, offset= 0.75 mm)

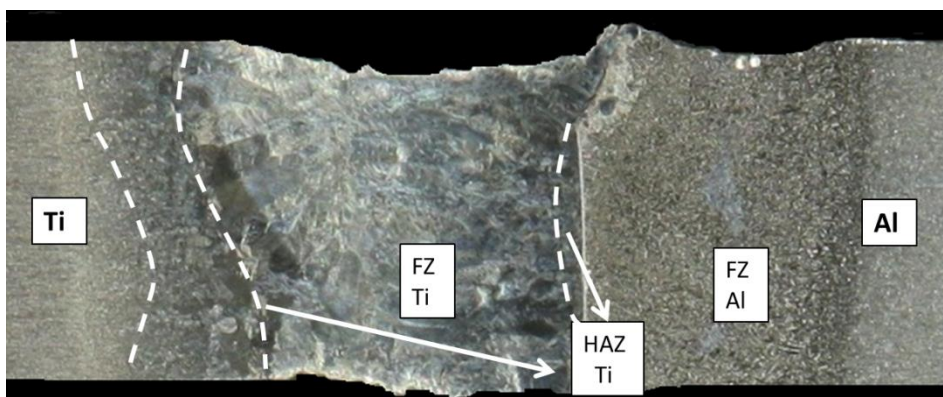


**Fig.4** Macrograph of sample 2 ( $P=1.20$  kW,  $v=2$  m/min,  $LE= 35.30$  J/mm, offset= 0.75 mm)

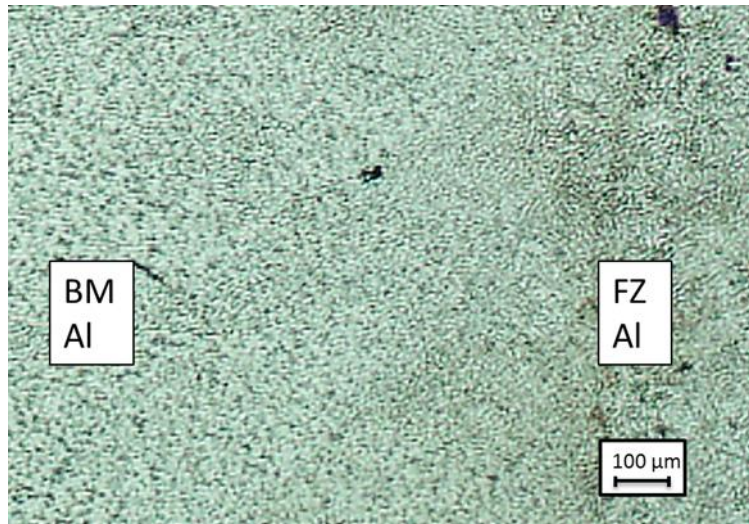


**Fig.5.** Microstructure of the Al side of sample 2 (P=1.20 kW, v=2 m/min, LE= 35.30 J/mm, offset= 0.75 mm).

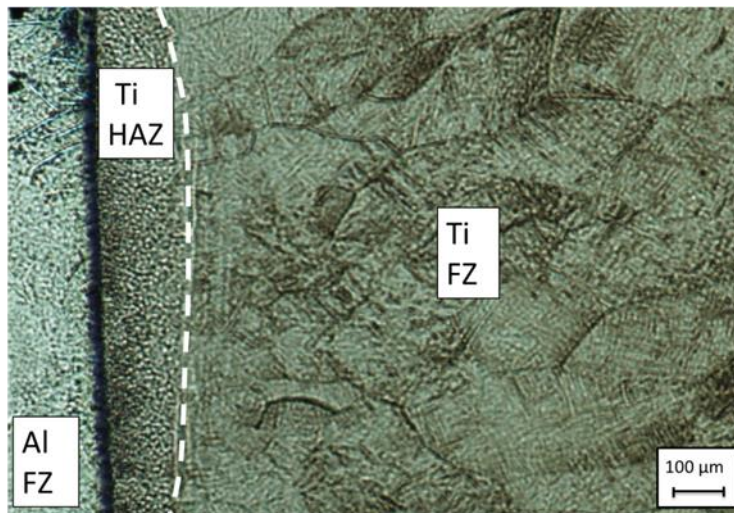


**Fig.6** Microstructure of the Ti side of sample 2 (P=1.20 kW, v=2 m/min, LE= 35.30 J/mm, offset= 0.75 mm)

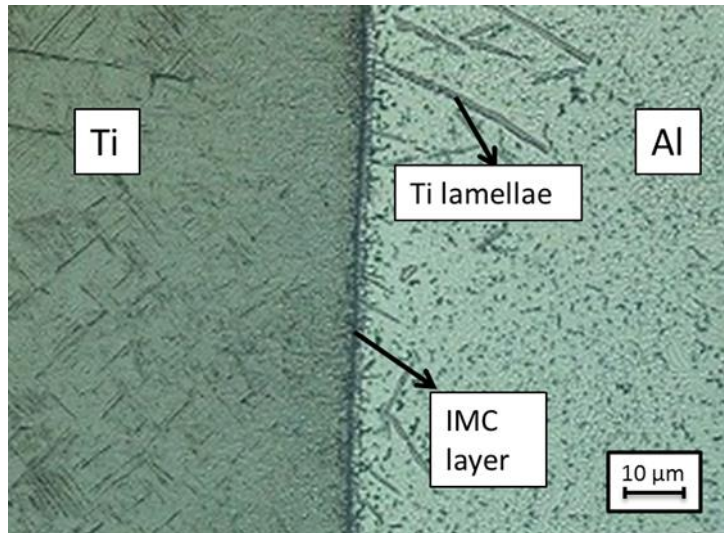


**Fig.7** IMC layer of sample 2 (P=1.20 kW, v=2 m/min, LE= 35.30 J/mm, offset= 0.75 mm)

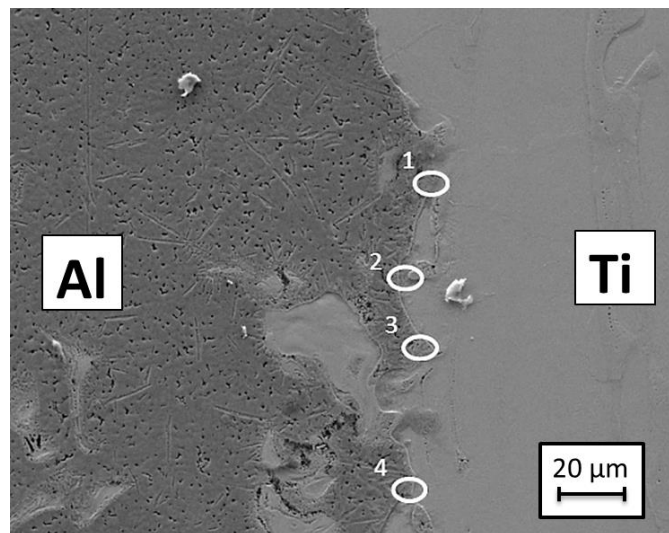


**Fig.8** IMC layer of sample 1 detected through SEM (P=1.20 kW, v=1 m/min, LE= 70.60 J/mm, offset= 0.75 mm)

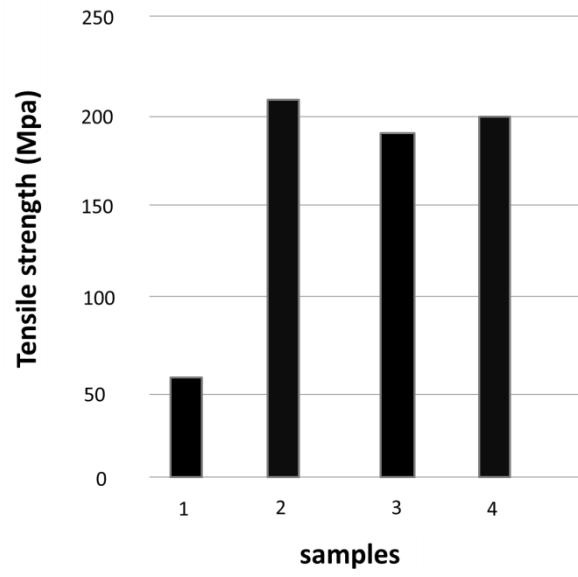


**Fig.9** Average values of tensile strength of samples

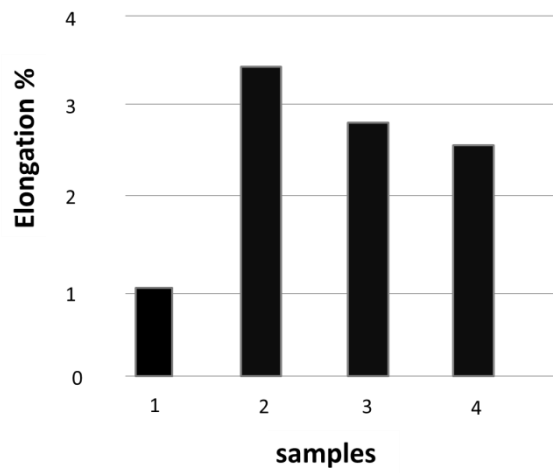


**Fig.10** Average values of elongation % of sample

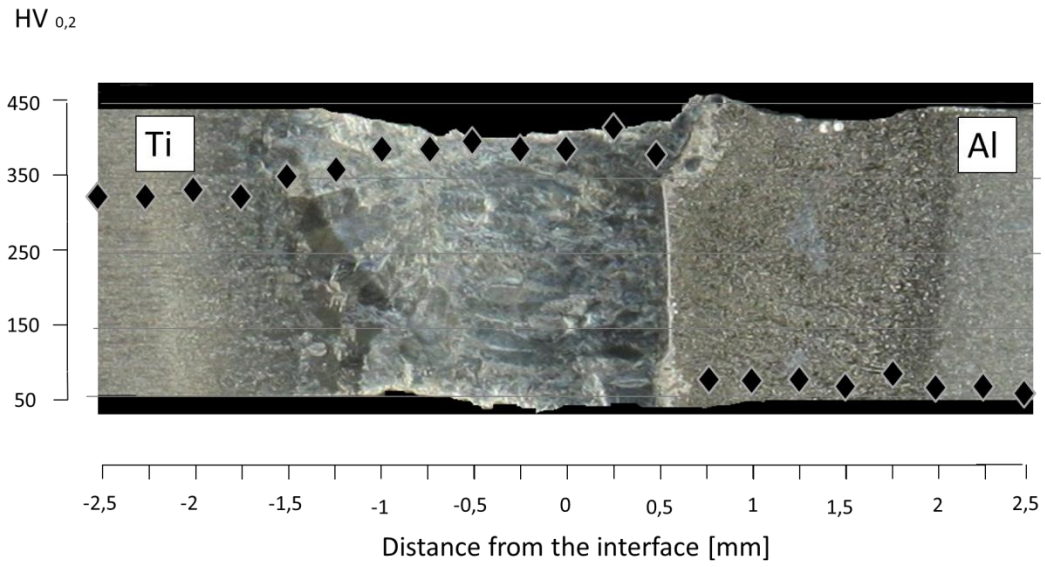


**Fig.11** Microhardness profile detected at the mid thickness

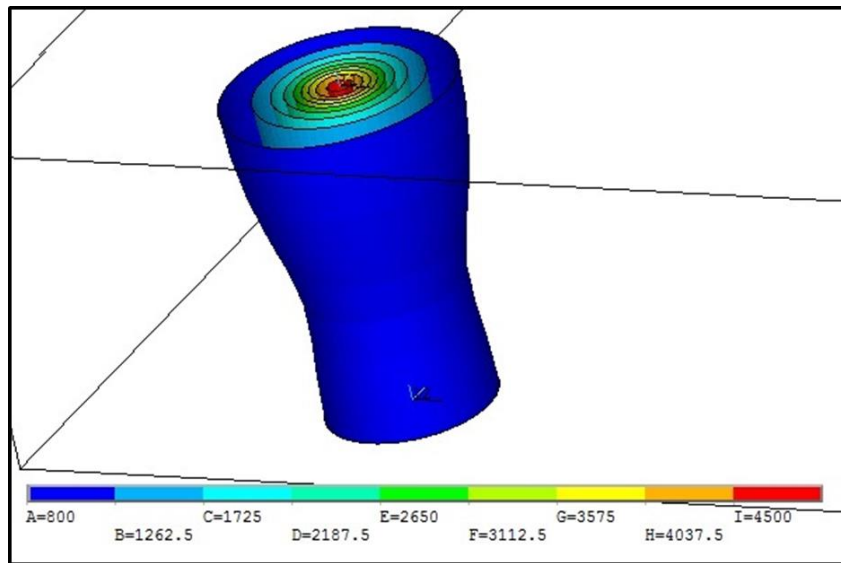


**Fig.12** Temperature fields for a singular thermal load application

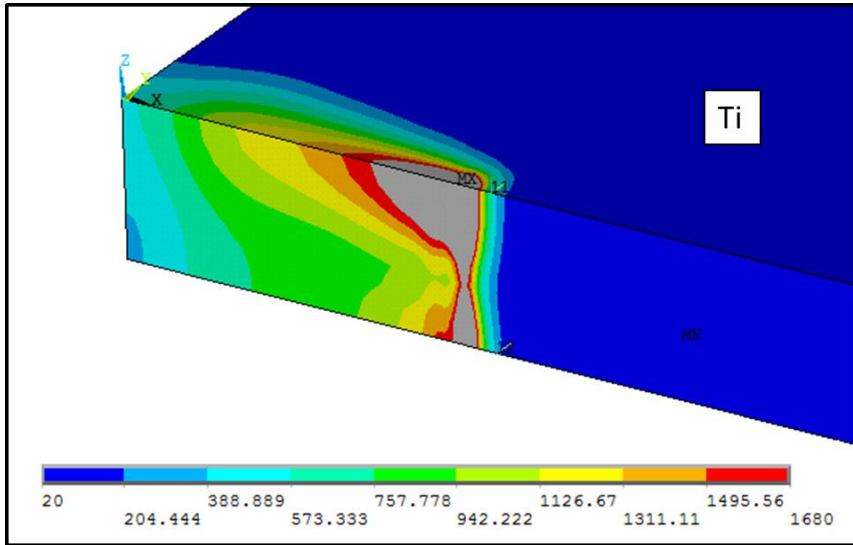


**Fig.13** Temperature distribution in the longitudinal plan under the condition of moving source

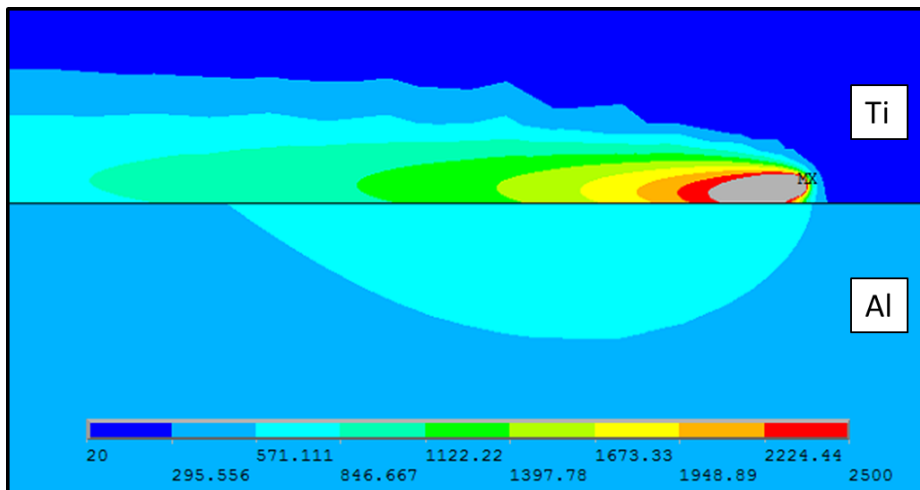


**Fig.14** Temperature fields on the top surface of the Al-Ti joint

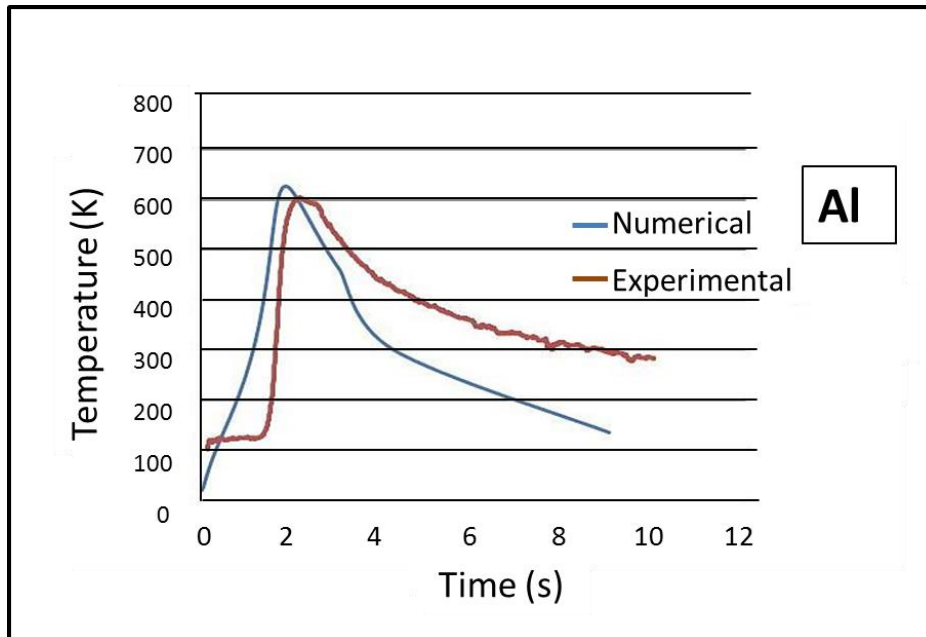


**Fig.15** Experimental and numerical thermal cycle for the Al side

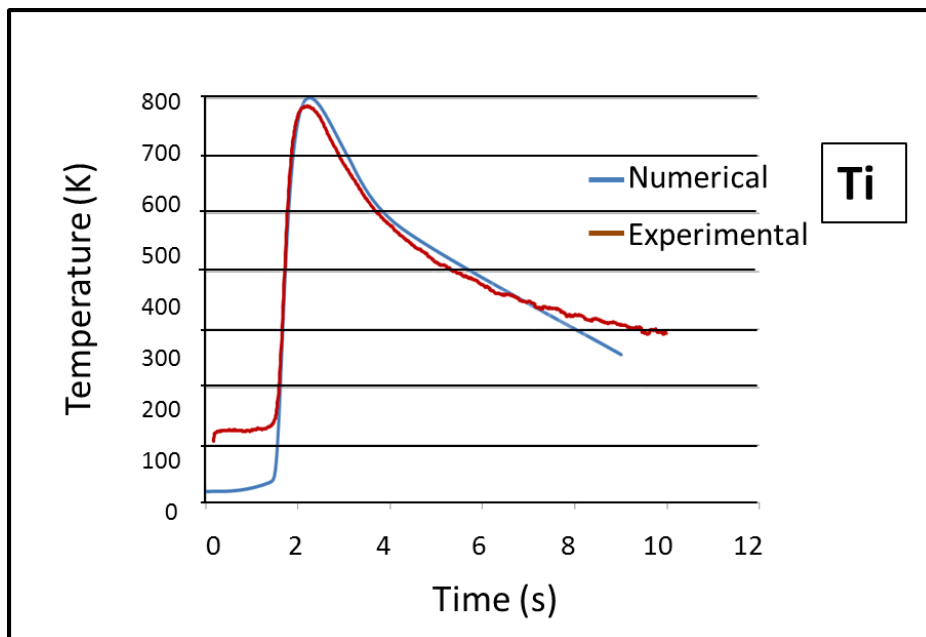


**Fig.16** Experimental and numerical thermal cycle for the Ti side

## List of captions

**Table 1** Chemical composition of the as-received materials (weight %).

**Table 2** Mechanical properties of the as-received materials: ultimate tensile strength (UTS), yield stress (YS), Young module (E), elongation to fracture % (A %), Vickers microhardness (HV).

**Table 3** Thermo-physical properties of the two base materials: thermal conductivity (K), melting temperature (T<sub>m</sub>), density (ρ).

**Table 4** Process parameters adopted.

**Table 5** Chemical composition of the zones indicated in figure 8.

**Table 1** Chemical composition of the as-received materials (weight %).

	Ti	Al	H	Fe	O	N	C	V	W	Other
<b>Ti6Al4V</b>	Balance	6.10	0.01	0.05	0.20	0.05	0.10	4.00	0.30	0.40

**Table 2** Mechanical properties of the as-received materials: ultimate tensile strength (UTS), yield stress (YS), Young module (E), elongation to fracture % (A %), Vickers microhardness (HV).

	UTS (MPa)	YS (MPa)	E (GPa)	A%	HV
<b>Ti6Al4V</b>	950	880	114	14	349
<b>AA5754</b>	230	80	68	17	62

**Table 3** Thermo-physical properties of the two base materials: thermal conductivity (K), melting temperature (T<sub>m</sub>), density (ρ).

	K (W/(m.K))	T <sub>m</sub> (k)	ρ (g/ cm <sup>3</sup> )
<b>Ti6Al4V</b>	6.7	1650	4.43
<b>AA5754</b>	147	870	2.66

**Table 4** Process parameters adopted.

Sample	Laser power (kW)	Welding speed (m/min)	Linear energy (J/mm)
1	1.20	1.00	70.60
2	1.20	2.00	35.30
3	1.50	2.50	35.70
4	1.50	3.00	30.00

**Table 5** Chemical composition of the zones indicated in figure 8.

<b>Zone</b>	<b>Al</b>	<b>Mg</b>	<b>Ti</b>	<b>V</b>
1	73.5	1.1	24.0	1.4
2	88.0	3.1	8.5	0.3
3	53.6	0.9	43.2	2.3
4	52.2	1.5	40.9	2.4